

¹For a survey of experimental work in this area up until 1955, see L. Marton, L. B. Leder, and H. Mendlowitz, in *Advances in Electronics and Electron Physics* (Academic, New York, 1955), Vol. 7; also, see L. Marton [Rev. Mod. Phys. 28, 172 (1956)] for a less detailed and more informal discussion.

²For an early review of the theoretical situation, see D. Pines, Rev. Mod. Phys. 28, 184 (1956).

³L. Marton, J. Phys. Soc. Jap. Suppl. 17, 68 (1962), see Fig. 4.

⁴J. P. Walter and M. L. Cohen, Phys. Rev. B 5, 3101 (1972).

⁵L. Marton, J. A. Simpson, H. A. Fowler, and N. Swanson, Phys. Rev. 126, 182 (1962).

⁶S. L. Adler, Phys. Rev. 126, 413 (1962).

⁷N. Wisner, Phys. Rev. 129, 62 (1963).

⁸H. Ehrenreich and M. H. Cohen, Phys. Rev. 115,

786 (1959).

⁹J. D. Jackson, *Classical Electrodynamics* (Wiley, New York, 1962).

¹⁰D. Pines and P. Nozières, *Theory of Quantum Liquids* (Benjamin, New York, 1966).

¹¹H. Watanabe, J. Phys. Soc. Jap. 11, 12 (1956).

¹²P. C. Martin and J. Schwinger, Phys. Rev. 115, 1392 (1959).

¹³D. F. DuBois and M. G. Kivelson, Phys. Rev. 186, 409 (1969).

¹⁴C. Kunz, Z. Phys. 167, 53 (1962).

¹⁵B. W. Ninham, C. J. Powell, and N. Swanson, Phys. Rev. 145, 209 (1966).

¹⁶C. V. Festenberg, Z. Phys. 207, 47 (1967).

¹⁷E. N. Foo and J. J. Hopfield, Phys. Rev. 173, 635 (1968).

Electron-Paramagnetic-Resonance Investigation of the Dynamic Jahn-Teller Effect in $\text{SrCl}_2:\text{Y}^{2+}$ and $\text{SrCl}_2:\text{Sc}^{2+}$

J. R. Herrington*[†] and T. L. Estle*

Physics Department, Rice University, Houston, Texas 77001

L. A. Boatner

Advanced Technology Center, Inc.,[‡] Dallas, Texas 75222

(Received 13 October 1972)

EPR spectra have been observed for $\text{SrCl}_2:\text{Y}^{2+}$ and $\text{SrCl}_2:\text{Sc}^{2+}$ at liquid-helium temperatures. At 1.2 K the spectra were dominated by anisotropic hyperfine patterns whose line shapes and angular dependences were explained using second-order solutions of the effective Hamiltonian for an isolated 2E_g state split by large random internal strains. Pronounced asymmetries in some of the strain-produced line shapes for $\text{SrCl}_2:\text{Sc}^{2+}$ are shown to result from second-order terms in the solution of the effective Hamiltonian. Coexisting with the anisotropic hyperfine patterns are weak nearly isotropic hyperfine patterns with typical line shapes. Variations in the apparent intensity of lines in these weak hyperfine patterns as functions of the applied-magnetic-field direction and temperature imply that these lines result from averaging by vibronic relaxation of a portion of the anisotropic pattern. This interpretation is further strengthened in the case of $\text{SrCl}_2:\text{Sc}^{2+}$ by the observation of a predicted anisotropy in the "averaged" spectrum. The effective-Hamiltonian parameters for $\text{SrCl}_2:\text{La}^{2+}$, $\text{SrCl}_2:\text{Y}^{2+}$, and $\text{SrCl}_2:\text{Sc}^{2+}$ are analyzed in terms of crystal field theory modified to include a weak to moderate vibronic interaction, i.e., a dynamic Jahn-Teller effect.

I. INTRODUCTION

For a nonlinear polyatomic complex Jahn and Teller¹ have shown that the orbital electronic degeneracy permitted by a symmetric nuclear configuration is incompatible with the stability of the symmetric configuration since asymmetric distortions remove the degeneracy and lower the energy of the system. For high-symmetry complexes in solids, e.g., ions with a d^1 configuration in eight-coordinated cubic sites, this instability is a result of the interaction between lattice vibrations and the electrons located on the ions. This vibrational-electronic or vibronic interaction determines the nature and the degeneracies of the states of the complex,

both of which will generally be different from the results for the electronic states in the absence of the vibronic interaction. This subject has been extensively investigated theoretically.²⁻⁴ When sufficiently strong, the vibronic interaction together with internal strains can produce a stable spontaneous distortion of the nuclear configuration to a symmetry sufficiently low to remove all orbital degeneracy, i.e., a "static" Jahn-Teller effect. However, even when the vibronic interaction is relatively weak, it produces pronounced effects on the matrix elements of certain vibronic operators and hence on certain experimental parameters, i.e., a "dynamic" Jahn-Teller effect. Since the existence of a significant vibronic interaction in-

validates the crystal field model, most experimental investigations have been directed toward finding instances where crystal field theory could not explain the observations. Ham⁴ and Sturge⁵ have reviewed all but the more recent experimental and theoretical developments in the study of the Jahn-Teller effect.

For orbital doublets only a limited amount of experimental data exists which permits definite inferences concerning the magnitude and nature of the vibronic coupling. This, together with the absence of systematic investigations and the restricted role experiment has played in verifying the substantial theoretical work, suggests the need for a more extensive experimental study of the Jahn-Teller effect and its implications concerning 2E states.

In our previous work⁶⁻⁹ concerning $\text{SrCl}_2:\text{La}^{2+}$ we have demonstrated that the ground vibronic state is an isolated doublet transforming like the $E_g(\Gamma_3^+)$ irreducible representation of O_h . This result, together with the observation that certain parameters were reduced from values predicted by crystal field theory (i. e., zero vibronic coupling), implied that the weak- to moderate-vibronic-coupling model developed extensively by Ham^{3,4} provided an accurate description of the $\text{SrCl}_2:\text{La}^{2+}$ system. This paper describes further EPR investigations of ions with 2E_g ground states. We report here our studies of $\text{SrCl}_2:\text{Y}^{2+}$ and $\text{SrCl}_2:\text{Sc}^{2+}$, which were the subject of a previous preliminary presentation.¹⁰

II. THEORY

The effective-Hamiltonian formalism for an isolated vibronic doublet has been developed and solved to first order by Ham.^{3,4} The importance of second-order terms in explaining EPR spectra was discussed previously in Ref. 8 (hereafter referred to as I). In this section the effective Hamiltonian will be reviewed and the solutions⁸ will be used as a starting point for discussions of line shapes and anisotropies of the EPR transitions observed for Sc^{2+} and Y^{2+} in SrCl_2 .

The effective Hamiltonian for an isolated 2E_g state^{3,4,8,9} in O_h symmetry is given in Eq. (1):

$$H = qV_s(e_\theta \mathcal{E}_\theta + e_\epsilon \mathcal{E}_\epsilon) + g_1 \mu_B \vec{H} \cdot \vec{S} \alpha_1 + A_1 \vec{I} \cdot \vec{S} \alpha_1 \\ + \frac{1}{2} qg_2 \mu_B [(3H_x S_x - \vec{H} \cdot \vec{S}) \mathcal{E}_\theta + \sqrt{3} (H_x S_x - H_y S_y) \mathcal{E}_\epsilon] \\ + \frac{1}{2} qA_2 [(3I_x S_x - \vec{I} \cdot \vec{S}) \mathcal{E}_\theta + \sqrt{3} (I_x S_x - I_y S_y) \mathcal{E}_\epsilon] \\ + \frac{1}{2} qQ [(3I_x I_x - \vec{I} \cdot \vec{I}) \mathcal{E}_\theta + \sqrt{3} (I_x I_x - I_y I_y) \mathcal{E}_\epsilon]. \quad (1)$$

The first term in the Hamiltonian represents the effects of internal strain or applied stress while the second and third terms are the isotropic Zeeman and hyperfine interactions. The last three terms are the anisotropic Zeeman, anisotropic hyperfine, and quadrupole interactions, respec-

tively. The quadrupole interaction has been treated elsewhere.⁹ The coupling coefficients qV_s , $g_1 \mu_B$, A_1 , $\frac{1}{2} qg_2 \mu_B$, $\frac{1}{2} qA_2$, and $\frac{1}{2} qQ$ in Eq. (1) represent the relative strengths of the different terms with the reduction factor^{3,4} included explicitly. The quantities \vec{H} , \vec{S} , and \vec{I} are, respectively, the applied magnetic field, the electronic-spin operator, and the nuclear-spin operator. The components of strain e_θ and e_ϵ are defined as $e_\theta = \frac{1}{2}(2e_{zz} - e_{xx} - e_{yy})$ and $e_\epsilon = \frac{1}{2}\sqrt{3}(e_{xx} - e_{yy})$, where e_{xx} , e_{yy} , and e_{zz} are the diagonal components of the strain tensor. Matrix representations of the vibronic operators α_1 , \mathcal{E}_θ , and \mathcal{E}_ϵ are given in Eq. (2) [note the upper-right-hand matrix elements are $\langle \theta | \mathcal{O} | \epsilon \rangle$, where $|\theta\rangle$ and $|\epsilon\rangle$ are vibronic basis functions which transform as do the $\theta(3x^2 - r^2)$ and $\epsilon(\sqrt{3}(x^2 - y^2))$ components of the E_g irreducible representation of the point group O_h].

$$\alpha_1 = \begin{pmatrix} 1 & 0 \\ 0 & 1 \end{pmatrix}, \quad \mathcal{E}_\theta = \begin{pmatrix} -1 & 0 \\ 0 & 1 \end{pmatrix}, \quad \mathcal{E}_\epsilon = \begin{pmatrix} 0 & 1 \\ 1 & 0 \end{pmatrix}. \quad (2)$$

Assuming that the strain determines the composition of vibronic states (see Appendixes A and B of I and Sec. VII of Ham³) the following second-order solution is easily obtained for the frequencies of the $\Delta M_S = \pm 1$, $\Delta M_I = 0$ transitions:

$$h\nu_{\pm} = \left(g_1 \pm \frac{1}{2} qg_2 f_1 + \frac{(qg_2)^2}{g_1} f_3 \right) \mu_B H \\ + \left(A_1 \pm \frac{1}{2} qA_2 f_1 + \frac{(qA_2)^2}{A_1} f_3 + 2 \frac{qg_2}{g_1} qA_2 f_3 \right. \\ \left. + \frac{4(qQ)^2}{A_1} [(f_3 - f_4) + 2(f_4 - 2f_3)I(I+1)] \right) M_I \\ + \left(\frac{(A_1 \mp \frac{1}{4} qA_2 f_1)^2}{2g_1 \mu_B H} + \frac{(qA_2)^2}{g_1 \mu_B H} f_4 \right) [(I+1) - M_I^2] \\ + \frac{(qA_2)^2}{g_1 \mu_B H} f_3 M_I^2 + \frac{8(qQ)^2}{A_1} (2f_3 - f_4) M_I^3. \quad (3)$$

The two signs refer to the two strain-produced Kramers doublets. The functions f_1 , f_3 , and f_4 are defined in Eqs. (4), (5) and (6):

$$f_1 = (3n^2 - 1) \cos \phi + \sqrt{3} (l^2 - m^2) \sin \phi, \quad (4)$$

$$f_3 = \frac{1}{8} \{ 2 - [(3n^2 - 1) \cos \phi + \sqrt{3} (l^2 - m^2) \sin \phi]^2 \\ - [-(3n^2 - 1) \cos 2\phi + \sqrt{3} (l^2 - m^2) \sin 2\phi] \}, \quad (5)$$

$$f_4 = \frac{1}{32} \{ 4 + [(3n^2 - 1) \cos \phi + \sqrt{3} (l^2 - m^2) \sin \phi]^2 \\ + 4 [-(3n^2 - 1) \cos 2\phi + \sqrt{3} (l^2 - m^2) \sin 2\phi] \}. \quad (6)$$

Here l , m , and n represent the direction cosines of the magnetic field with respect to the cubic axes and $\tan \phi = e_\epsilon / e_\theta$. The notation used here is the same as that used in I. Equations (5) and (6) are equivalent to the corresponding equations for f_3 and f_4 in I. The notation in Ref. 9 is somewhat different.

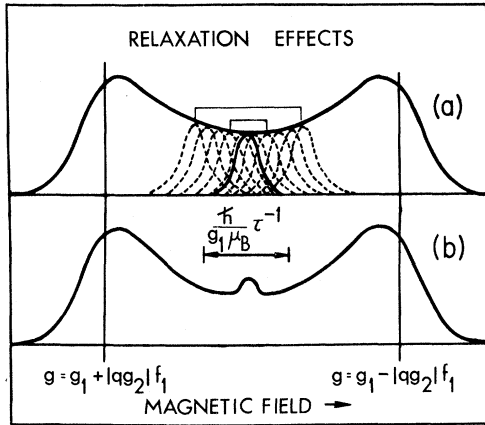


FIG. 1. (a) The line shape in first order produced by the distribution in the angle ϕ given by $\tan\phi = e_c/e_g$. EPR signals occur in pairs, equidistant from the center of the envelope. (b) The effect of rapid vibronic relaxation is to average those pairs of transitions whose frequency differences $[\nu_+ - \nu_-]$ of Eq. (3) are less than the vibronic relaxation rate τ^{-1} . Hence, as the relaxation rate increases with temperature, that portion of the envelope that is averaged increases. In addition, rotation of the magnetic field in a $\{110\}$ plane toward a $\langle 111 \rangle$ axis reduces the value of the function f_1 to zero as shown in Eq. (4). Hence, as the field gets closer to a $\langle 111 \rangle$ direction, more transitions satisfy the condition $\tau^{-1} > \nu_+ - \nu_-$ and the "averaged" line increases in intensity. The absorption is shown schematically as a function of applied magnetic field with the extremes of the envelope designated by vertical lines and labeled with effective first-order g factors.

Using crystal field theory and assuming that the spin-orbit interaction is very small with respect to the cubic crystal field interaction, i. e., $\lambda/\Delta \ll 1$, closed perturbation expressions may be

$$\begin{aligned} h\nu = & \left(g_1 + \frac{(qg_2)^2}{g_1} f_3 \right) \mu_B H + \left(A_1 + \frac{(qA_2)^2}{A_1} f_3 + \frac{2qg_2}{g_1} qA_2 f_3 + \frac{4(qQ)^2}{A_1} [(f_3 - f_4) + 2(f_4 - 2f_3)I(I+1)] \right) M_I \\ & + \left(\frac{A_1^2}{2g_1\mu_B H} + \frac{(qA_2 f_1)^2}{32g_1\mu_B H} + \frac{(qA_2)^2}{g_1\mu_B H} f_4 \right) [I(I+1) - M_I^2] + \frac{(qA_2)^2}{g_1\mu_B H} f_3 M_I^2 + \frac{8(qQ)^2}{A_1} (2f_3 - f_4) M_I^3. \quad (12) \end{aligned}$$

Equation (12) gives the average of $h\nu_+$ and $h\nu_-$ for a given value of H . When the second-order terms in Eq. (12) are negligible, averaging by relaxation produces an isotropic hyperfine pattern, each component of which is located midway between the two extremes of the appropriate envelope. This situation is shown schematically in Fig. 1(b) and characterizes the case of $\text{SrCl}_2:\text{La}^{2+}$. If A_1 and A_2 are comparable, then the $(qA_2)^2/A_1$ term is important and the "averaged" spectrum will be slightly anisotropic. This is the case for $\text{SrCl}_2:\text{Sc}^{2+}$ which

derived for the parameters g_1 , g_2 , A_1 , A_2 , and Q in Eqs. (1) and (3). These expressions are given in Eqs. (7)–(11) for a single d electron:

$$g_1 = 2.0023 - 4\lambda/\Delta, \quad (7)$$

$$g_2 = -4\lambda/\Delta = g_1 - 2.0023, \quad (8)$$

$$A_1 = (-2\mu_B\mu\langle r^{-3} \rangle/I)(\kappa + 4\lambda/\Delta), \quad (9)$$

$$A_2 = (-2\mu_B\mu\langle r^{-3} \rangle/I)\left(\frac{4}{7} + \frac{34}{7}\lambda/\Delta\right), \quad (10)$$

$$Q = \frac{2e^2 Q_N}{7I(2I-1)} \langle r^{-3} \rangle. \quad (11)$$

Here λ , Δ , μ_B , μ , I , $\langle r^{-3} \rangle$, κ , e , and Q_N are, respectively, the spin-orbit coupling constant, the cubic crystal field splitting $10Dq$, the Bohr magneton, the nuclear magnetic dipole moment, the nuclear spin, the one-electron expectation value of r^{-3} , the Fermi contact parameter, the electron charge, and the nuclear electric quadrupole moment. One immediately notes from Eqs. (9) and (10) that when κ is small, as it is for the $3d^1$ configuration, then $A_2 \approx A_1$, and terms in Eq. (3) of the form $(qA_2)^2/A_1$ are extremely important. These terms can have pronounced effects on the EPR line shapes and will be discussed in greater detail for $\text{SrCl}_2:\text{Sc}^{2+}$ in Sec. III B.

As pointed out by Ham,^{3,4} rapid vibronic relaxation results in averaging of a portion of the strain-produced EPR line shapes. The first-order effects of such averaging on the EPR spectrum of $\text{SrCl}_2:\text{La}^{2+}$ were discussed in I and are illustrated schematically in Fig. 1(a). If the relaxation rate τ^{-1} for the vibronic process is much greater than the difference between the two frequencies ν_+ and ν_- and both Kramers doublets are equally populated (i. e., the strain splitting δ satisfies $\delta \ll kT$), then an EPR signal will appear at the position $h\nu$ given in Eq. (12):

will be discussed further in Sec. III B.

III. EXPERIMENTAL RESULTS AND DISCUSSION

Single crystals of $\text{SrCl}_2:\text{Y}$ and $\text{SrCl}_2:\text{Sc}$ were grown from the melt using a vertical Bridgman technique described in I. The dopants were introduced as YCl_3 and ScCl_3 . Strong fluorescence was observed in the "as-grown" crystals using short-wavelength uv ($\lambda = 2537 \text{ \AA}$) excitation, but EPR was not observed until the crystals were reduced. Reduction resulted from exposure to γ rays

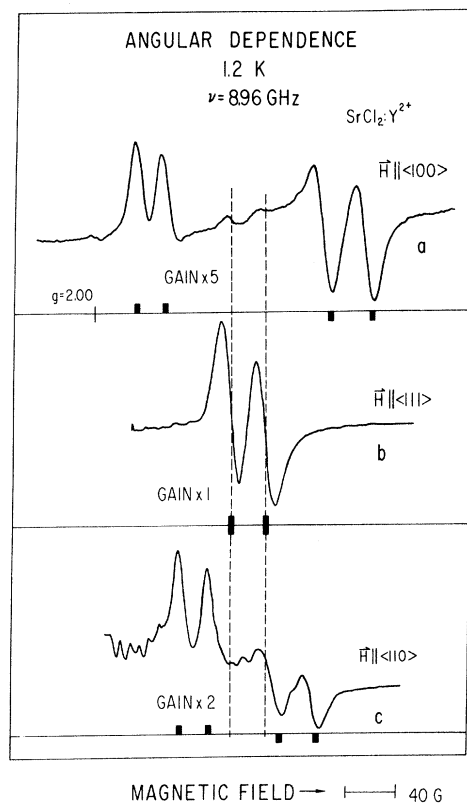


FIG. 2. The angular dependence of the EPR spectrum observed for a reduced $\text{SrCl}_2:\text{Y}$ single crystal; (a) $\vec{H} \parallel \langle 100 \rangle$, (b) $\vec{H} \parallel \langle 111 \rangle$, and (c) $\vec{H} \parallel \langle 110 \rangle$. The first derivative of absorption is shown versus magnetic field. Extremes of the two overlapping envelopes are identified by small vertical bars below each trace. The dashed vertical lines designate the positions of the two transitions for $\vec{H} \parallel \langle 111 \rangle$ and aid in identifying the lines produced by rapid vibronic relaxation. A large number of anisotropic lines, best seen for $\vec{H} \parallel \langle 110 \rangle$, were observed. These lines saturated easily and hence were not associated with the isolated Y^{2+} imperfections.

from a high-flux Cs^{137} source ($\sim 10^7$ rad) or by heating in Sr vapor (590°C for 15 min). The radiation produced a deep-red color in the $\text{SrCl}_2:\text{Y}$ crystals but $\text{SrCl}_2:\text{Sc}$ crystals remained colorless. Reduction in a Sr vapor produced a dark metallic sheen for both $\text{SrCl}_2:\text{Y}$ and $\text{SrCl}_2:\text{Sc}$ crystals similar to that observed for $\text{SrCl}_2:\text{La}^{2+}$.

EPR spectra were observed using a back-reflection homodyne spectrometer operating at about 9 GHz. Precise orientations were obtained using independent orthogonal rotations of both the applied magnetic field and the crystal.

A. $\text{SrCl}_2:\text{Y}^{2+}$

The EPR spectrum observed at 1.2 K for a reduced $\text{SrCl}_2:\text{Y}$ single crystal is shown in Fig. 2 for the applied magnetic field parallel to the $\langle 100 \rangle$,

$\langle 111 \rangle$, and $\langle 110 \rangle$ crystallographic directions. This spectrum is simpler than that of $\text{SrCl}_2:\text{La}^{2+}$ in I because the nuclear spin for the 100% naturally abundant isotope ^{89}Y is $\frac{1}{2}$.

The spectrum consists basically of two overlapping envelopes of transitions, each with the line shape characteristic of random internal strains.^{3,4} A schematic diagram of these two overlapping envelopes is shown in Fig. 3(a). The dotted curve represents one of the envelopes ($M_I = -\frac{1}{2}$) and the dashed curve represents the other ($M_I = +\frac{1}{2}$). The curves were calculated for $\vec{H} \parallel \langle 100 \rangle$ using Eq. (3) and the parameters listed in Table I for $\text{SrCl}_2:\text{Y}^{2+}$. Each value of ϕ was assumed to occur with equal probability thus producing two δ -function lines [one for the upper sign and one for the lower sign

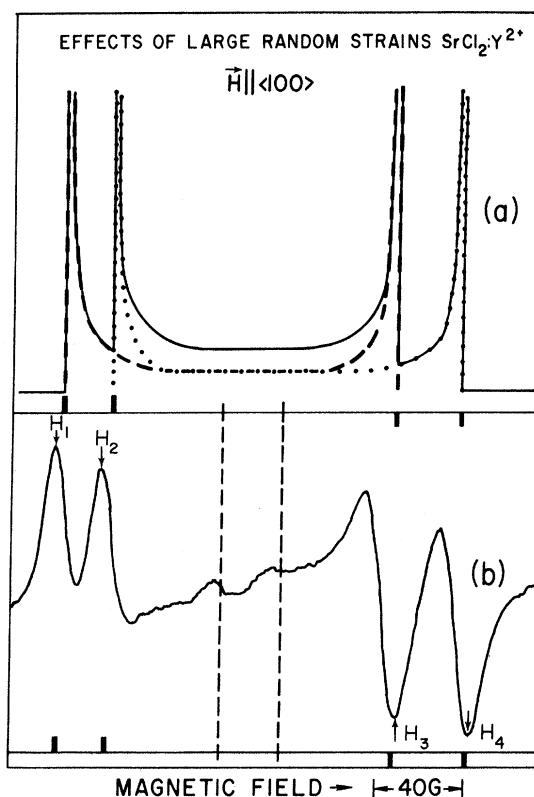


FIG. 3. (a) A schematic representation of the density of EPR transitions as a function of applied magnetic field. These were calculated using Eq. (3) assuming that all values of ϕ occur with equal probability. The dotted curve represents the $M_I = -\frac{1}{2}$ envelope and the dashed curve represents the $M_I = +\frac{1}{2}$ envelope. The solid curve results from adding the dashed and dotted curves. The envelope extremes are shown as small vertical bars below the curves. (b) The first-derivative presentation of absorption versus magnetic field observed for a reduced $\text{SrCl}_2:\text{Y}$ single crystal. The dashed vertical lines locate the two lines produced by averaging a portion of the anisotropic pattern. The extremes of the two envelopes are shown as small vertical bars below the trace.

TABLE I. Effective Hamiltonian parameters measured for Sc^{2+} , Y^{2+} , and La^{2+} in SrCl_2 . The signs have been chosen consistent with predictions of crystal field theory and sign relations implied by the data analysis.

System	g_1	gg_2	A_1 (10^{-4} cm^{-1})	qA_2 (10^{-4} cm^{-1})	qQ (10^{-4} cm^{-1})
$\text{SrCl}_2 : \text{Sc}^{2+}$	$+1.9531 \pm 0.0010^a$	-0.0442 ± 0.0008^a	-62.7 ± 0.8^a	-31.5 ± 0.8^a	-0.20 ± 0.05^b
$\text{SrCl}_2 : \text{Y}^{2+}$	$+1.9289 \pm 0.0010^a$	-0.0478 ± 0.0008^a	$+24.3 \pm 0.8^a$	$+5.0 \pm 0.8^a$...
$\text{SrCl}_2 : \text{La}^{2+}$	$+1.8808 \pm 0.0010^c$	-0.0687 ± 0.0008^c	-119.5 ± 0.8^c	-18.8 ± 0.8^c	$+0.15 \pm 0.05^b$

^aThis paper.

^bReference 9.

^cReference 8.

in Eq. (3)]. The solid curve is the sum of the dotted and dashed curves. The extremes of the two envelopes (located by small vertical bars below the curves) are the field positions predicted by Eq. (3) for $\phi = 0^\circ$. The primary effect of considering each line to have a nonzero width is to broaden the extremes as shown in I. In Fig. 3(b) the observed first-derivative presentation of absorption versus magnetic field is shown for $\vec{H} \parallel \langle 100 \rangle$. The evaluation of the coupling coefficients g_1 , qg_2 , A_1 , and qA_2 in Eq. (3) (note that the quadrupole interaction vanishes for $I = \frac{1}{2}$) is simplified for $\vec{H} \parallel \langle 100 \rangle$ since $f_3 = 0$ and $f_4 = 0$ at the extremes. A first-order estimate of these parameters can easily be obtained using Eqs. (13)–(16) and the measured field position of the four peaks shown in Fig. 3(b) and labeled H_1 , H_2 , H_3 , and H_4 :

$$g_1 = \frac{\nu/c}{(H_1 + H_2) \mu_B / hc} + \frac{\nu/c}{(H_3 + H_4) \mu_B / hc}, \quad (13)$$

$$qg_2 = -\frac{\nu/c}{(H_1 + H_2) \mu_B / hc} + \frac{\nu/c}{(H_3 + H_4) \mu_B / hc}, \quad (14)$$

$$A_1 \text{ (cm}^{-1}\text{)} = -\left(\frac{H_1 - H_2}{H_1 + H_2} + \frac{H_3 - H_4}{H_3 + H_4} \right) \frac{\nu}{c}, \quad (15)$$

$$qA_2 \text{ (cm}^{-1}\text{)} = \left(\frac{H_1 - H_2}{H_1 + H_2} - \frac{H_3 - H_4}{H_3 + H_4} \right) \frac{\nu}{c}. \quad (16)$$

A more accurate set of parameters is obtained when the field positions H_1 to H_4 are modified to allow for second-order terms. In addition, corrections for the nonzero width of the individual resonances, following the prescription in I, are required. The iteratively refined values for these four parameters are listed in Table I and were used in Eq. (3) to compute the angular dependence of the extremes. These computed extremes are plotted as solid lines in Fig. 4. The open circles are the experimental values obtained using magnetic field positions of the peaks in the first-derivative presentation of absorption and correcting for component linewidth as discussed in I. The fit is excellent considering the uncertainty in positions of the true extremes of the envelopes.

As seen in Fig. 2(a), a pair of lines which are isotropic to within experimental error were ob-

served to coexist with the anisotropic pattern discussed above. These lines increased in apparent intensity (the peak-to-peak amplitude in a first-derivative presentation) as the applied magnetic field was rotated in a $\{110\}$ plane toward a $\langle 111 \rangle$ direction. This angular variation in the intensities of these lines suggests that they result from averaging of a portion of the anisotropic pattern. As the temperature was increased, the intensities of these lines increased and the peaks in the first-derivative presentation of the anisotropic pattern broadened, again suggesting averaging by vibronic relaxation. The temperature dependence of the EPR spectrum for $\vec{H} \parallel \langle 100 \rangle$ is shown in Fig. 5. The approximately linear increase with temperature of the intensities of these two lines implies that the vibronic relaxation rate τ^{-1} is also increasing approximately linearly with temperature (characteristic of the direct process). This behavior was also observed for $\text{SrCl}_2 : \text{La}^{2+}$ (see I).

The features discussed above were generally independent of incident microwave power, but a large number of anisotropic lines which saturated easily were also observed [see Fig. 2(c) in particular]. Owing to their saturation behavior, these lines were not associated with isolated Y^{2+} and, therefore, were not analyzed.

B. $\text{SrCl}_2 : \text{Sc}^{2+}$

The EPR spectrum observed at 4.2 K for a reduced $\text{SrCl}_2 : \text{Sc}$ single crystal is shown in Fig. 6 for the applied magnetic field parallel to the $\langle 100 \rangle$, $\langle 111 \rangle$, and $\langle 110 \rangle$ crystallographic directions. The dominant pattern is composed of eight anisotropic hyperfine envelopes since the nuclear spin of the 100% naturally abundant isotope ^{45}Sc is $\frac{7}{2}$. In Fig. 6 the extremes for the envelopes are indicated by small vertical bars below each trace. The coupling coefficients g_1 , qg_2 , A_1 , and qA_2 were determined using the least-squares procedure outlined in I and the spectrum obtained for $\vec{H} \parallel \langle 100 \rangle$. The values of these parameters are listed in Table I. The quadrupole coupling parameter qQ was evaluated from the $\Delta M_I = \pm 1$ transitions for $\vec{H} \parallel \langle 111 \rangle$ as described previously.⁹ These parameters were then used in Eq. (3) to compute the angular dependence of the extremes for each envelope. These calculated ex-

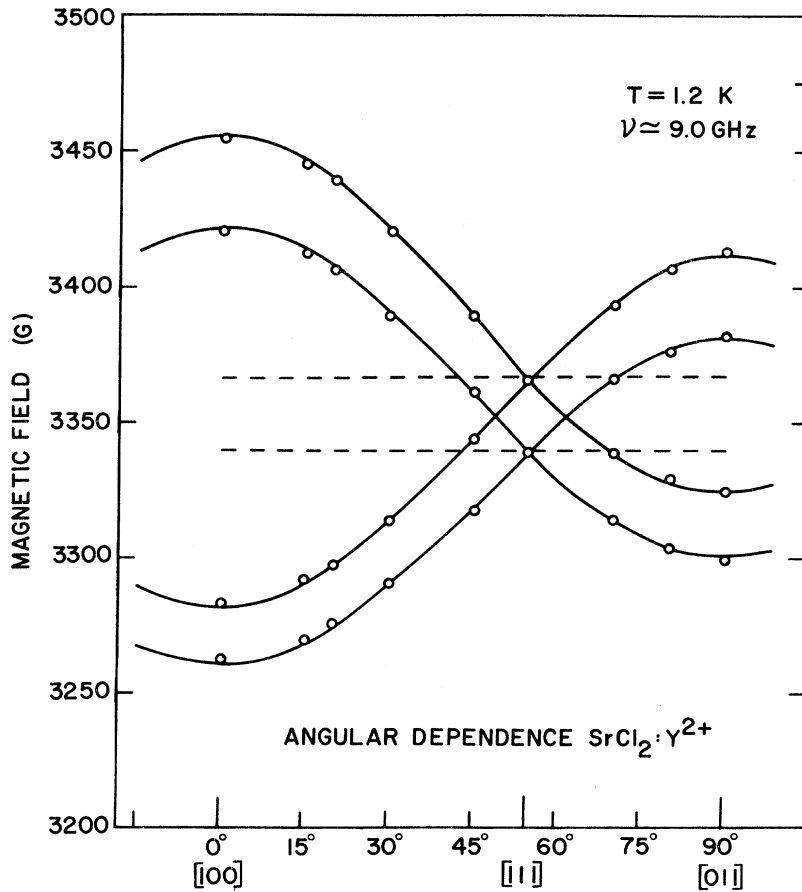


FIG. 4. The angular dependence of the extremes in the EPR spectrum observed for $\text{SrCl}_2:\text{Y}^{2+}$. The solid lines were calculated using Eq. (3) together with the parameters listed in Table I for $\text{SrCl}_2:\text{Y}^{2+}$. The open circles represent experimental measurements. The dashed lines indicate the location of the "averaged" lines.

extremes are shown as solid lines in Fig. 7. The open circles designate the measured extremes. The weak lines located approximately midway between adjacent hyperfine lines for $\vec{H} \parallel \langle 111 \rangle$ [see Fig. 6(b)] are the $\Delta M_I = \pm 1$ "forbidden" transitions.⁹

A careful examination of Fig. 6(c), i. e., $\vec{H} \parallel \langle 110 \rangle$, reveals pronounced asymmetries of the envelopes, particularly those at the low-field end. For these envelopes the low-field extremes are sharper than the high-field extremes. This asymmetry was observed to be largest for $\vec{H} \parallel \langle 110 \rangle$ and seemed to be entirely absent for $\vec{H} \parallel \langle 100 \rangle$. This behavior is a result of the $(qA_2)^2/A_1$ term discussed in Sec. II. The origin of this asymmetry is shown schematically in Fig. 7. The dashed curves locate the position of the median transition of each of the eight envelopes, i. e., $\phi = 90^\circ$ for a $\{110\}$ plane. Half of the lines composing each envelope must lie between the appropriate dashed line and the high-field extreme of that envelope and half must lie between the dashed line and the low-field extreme. Thus, one sees from the dashed lines in Fig. 7 that with $\vec{H} \parallel \langle 110 \rangle$ the low-field extreme should be much sharper than the high-field extreme for the lowest

three envelopes. The asymmetry is a maximum for $\vec{H} \parallel \langle 110 \rangle$ and apparently absent for $\vec{H} \parallel \langle 100 \rangle$ because the function f_3 in Eq. (5) is zero for $\vec{H} \parallel \langle 100 \rangle$ and a maximum for $\phi = 90^\circ$ when \vec{H} is along $\langle 110 \rangle$.

The temperature dependence of a portion of the EPR spectrum for a reduced $\text{SrCl}_2:\text{Sc}$ sample is shown in Fig. 8. Traces (a), (b), and (c) correspond to progressively increasing temperature. As the temperature increased from 4.2 K, the anisotropic pattern was observed to broaden while a weak eight-line pattern emerged. The intensities of the components of this weak pattern (located by solid vertical lines in Fig. 8) increased approximately linearly with temperature whereas the peaks in the anisotropic pattern near the envelope extremes broadened with increasing temperature. In addition, for a constant temperature the apparent intensity of each weak line increased as the applied magnetic field was rotated in a $\{110\}$ plane toward a $\langle 111 \rangle$ direction. These characteristics imply that the origin of the weak pattern is averaging of a portion of the anisotropic pattern by direct vibronic relaxation. This interpretation was further strengthened by the observation that the positions

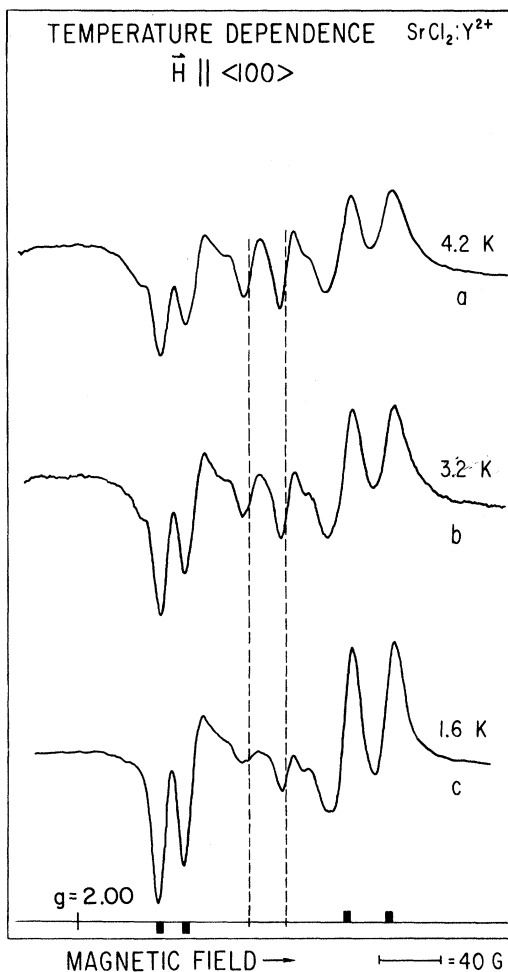


FIG. 5. The temperature dependence of the EPR spectrum from a reduced $\text{SrCl}_2:\text{Y}$ single crystal with $\vec{H} \parallel \langle 100 \rangle$, (a) 4.2, (b) 3.2, and (c) 1.6 K. The dashed vertical lines identify the lines produced by averaging resulting from vibronic relaxation. The first derivative of absorption versus magnetic field is shown and the extremes for the two envelopes are designated by small vertical bars at the bottom of the figure.

of these lines for $\vec{H} \parallel \langle 100 \rangle$ differed by a measurable amount from the position of the eight hyperfine lines observed for $\vec{H} \parallel \langle 111 \rangle$ (denoted in Fig. 8 by the broken vertical lines). In particular, for $\vec{H} \parallel \langle 100 \rangle$ these lines were located at positions halfway between the extremes (i. e., the dashed lines in Fig. 7). It is exactly this type of anisotropy (both in magnitude and sense) that is predicted by Eqs. (12) and (4)–(6) for $\vec{H} \parallel \langle 100 \rangle$ and $\vec{H} \parallel \langle 111 \rangle$. The observation of this anisotropy is additional evidence that averaging by rapid vibronic relaxation produces this weak pattern. These arguments are somewhat more complicated for \vec{H} along directions other than $\langle 111 \rangle$ or $\langle 100 \rangle$. For these general directions the averaged line is distributed between

the dashed and dotted lines in Fig. 7 in a manner which depends on the magnitude of the vibronic relaxation rate. For a small τ^{-1} only the lines corresponding to values of ϕ very close to 90° (the dashed lines in Fig. 7) will average. If τ^{-1} is much larger than the difference in frequency of the extremes, then all lines will be averaged. The dotted line in Fig. 7 corresponds to the position of the average of the two lines located at the extremes, that is, a value of ϕ very close to 0° or 180° .

We wish to emphasize two differences that exist between the EPR spectra observed for $\text{SrCl}_2:\text{Sc}^{2+}$ and $\text{SrCl}_2:\text{Y}^{2+}$. First, pronounced asymmetries which are present in the line shapes for $\text{SrCl}_2:\text{Sc}^{2+}$ for certain orientations of the applied magnetic field were not observed for $\text{SrCl}_2:\text{Y}^{2+}$. Second, while the pattern produced by rapid vibronic relaxation for $\text{SrCl}_2:\text{Y}^{2+}$ was isotropic within experimental error, that observed for $\text{SrCl}_2:\text{Sc}^{2+}$ exhibited a characteristic anisotropy in the hyperfine splitting. These differences occur because qA_2 is comparable to A_1 for Sc^{2+} . These features, together with many other details of the angular dependence, the line shapes, the forbidden hyperfine transitions, and the temperature dependence, are all consistent with the assumption of an isolated 2E_g state.

IV. IMPLICATIONS OF THE VIBRONIC MODEL

The EPR spectra reported for $\text{SrCl}_2:\text{La}^{2+}$ in I and for $\text{SrCl}_2:\text{Y}^{2+}$ and $\text{SrCl}_2:\text{Sc}^{2+}$ in this paper have been analyzed in terms of an effective Hamiltonian representing various interactions for an isolated 2E_g state. Such a state is predicted by crystal-field theory to be the orbital ground state for a d^1 configuration in eightfold cubic coordination. Ham^{3,4} has shown that the symmetry classification of the ground vibronic state for a weak to moderate vibronic interaction is also 2E_g . The only evidence that a vibronic interaction exists in the weak- to moderate-vibronic-coupling approximation is furnished by the observation that certain parameters in the effective Hamiltonian are reduced from the values predicted by crystal-field theory. It is the purpose of this section to demonstrate that a reduction of the effective-Hamiltonian parameters does indeed occur for the three systems $\text{SrCl}_2:\text{La}^{2+}$, $\text{SrCl}_2:\text{Y}^{2+}$, and $\text{SrCl}_2:\text{Sc}^{2+}$ and that the implied variations in the strength of the vibronic coupling are physically reasonable.

The reduction factor q included explicitly in the qg_2 , qA_2 , and qQ parameters may be estimated most easily from Eqs. (7) and (8) and the parameters g_1 and qg_2 listed in Table I. The results of these estimates are shown in Table II. As pointed out by Ham,^{3,4} the reduction factors can be correlated with the strength of the vibronic interaction. In particular, the smaller the reduc-

TABLE II. Vibronic-model parameters. For the most part these are not measured parameters but rough estimates or approximate fits to the simple vibronic model employed.

Parameter	SrCl ₂ : Sc ²⁺	SrCl ₂ : Y ²⁺	SrCl ₂ : La ²⁺
q	0.86	0.65	0.57
$E_{JT}/\hbar\omega$	0.1	0.5	1.0
V_{JT} (cm ⁻¹)	2000	5000	7000
qV_s (cm ⁻¹)	7000	13 000	15 000
δ (cm ⁻¹) ^a	0.7 to 0.07	1.3 to 0.13	1.5 to 0.15
τ^{-1} (sec ⁻¹) ^b	5×10^8	4×10^8	9×10^8
Δ (cm ⁻¹) ^c	6000	15 000	20 000
$\mu(\mu_N)$ ^d	5(4.75)	-0.2 (-0.14)	2.5 (2.76)
$\langle r^{-3} \rangle$ (10 ²² G ² /erg)	0.5	0.6	0.7
κ	1.0	2.0	2.5
$Q_N(b)$ ^d	-0.3 (-0.22)	...	+0.3 (+0.2)

^aThe first number is the strain splitting computed using a strain of 10⁻⁴ and the second is for a strain of 10⁻⁵.

^b $T = 20$ K.

^cThe spin-orbit coupling constants used in obtaining Δ were roughly 10% below the free ion values.

^dNumbers in parentheses are currently accepted values.

tion factor, the larger the ratio of the Jahn-Teller energy E_{JT} to the phonon energy $\hbar\omega$. Using the calculations of Longuet-Higgins *et al.*,² estimates of the ratio $E_{JT}/\hbar\omega$ were made and are listed in Table II. Using a value of 300 cm⁻¹ for $\hbar\omega$ (the approximate energy of the optical phonons in SrCl₂) the estimates of the vibronic-coupling coefficients V_{JT} listed in Table II were made. From the relationship between the vibronic-coupling coefficient and the strain-coupling coefficient⁴ estimates of V_s were made and multiplied by the appropriate reduction factors. These approximate results are listed in Table II. The variations in q and the parameters $E_{JT}/\hbar\omega$, V_{JT} , and qV_s are reasonable in view of the radial extent of d -electron wave functions. A $3d$ electron should be less extended than a $4d$ or $5d$ electron and better shielded from its surroundings. Thus, an ion with an incomplete $3d$ shell should be less sensitive to motions of the ligands. The vibronic interaction

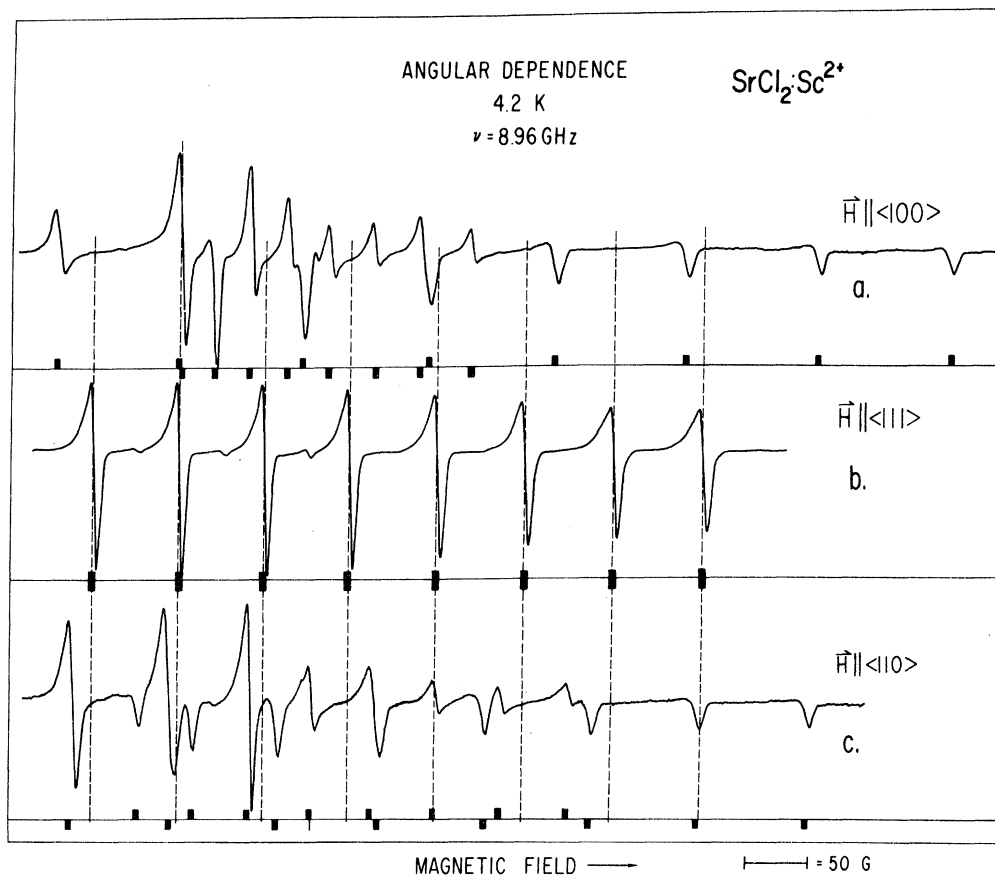


FIG. 6. The angular dependence of the EPR spectrum observed for a reduced SrCl₂:Sc single crystal: (a) $\vec{H} \parallel \langle 100 \rangle$, (b) $\vec{H} \parallel \langle 111 \rangle$, and (c) $\vec{H} \parallel \langle 110 \rangle$. The first derivative of absorption versus magnetic field is shown. Extremes of the eight anisotropic envelopes are designated by small vertical bars below each trace. The dashed vertical lines denote the positions of the eight collapsed envelopes for $\vec{H} \parallel \langle 111 \rangle$. Note that they do not lie halfway between the two extremes for each envelope for $\vec{H} \parallel \langle 100 \rangle$. Note also the pronounced asymmetry of the lowest three envelopes of transitions for $\vec{H} \parallel \langle 110 \rangle$.

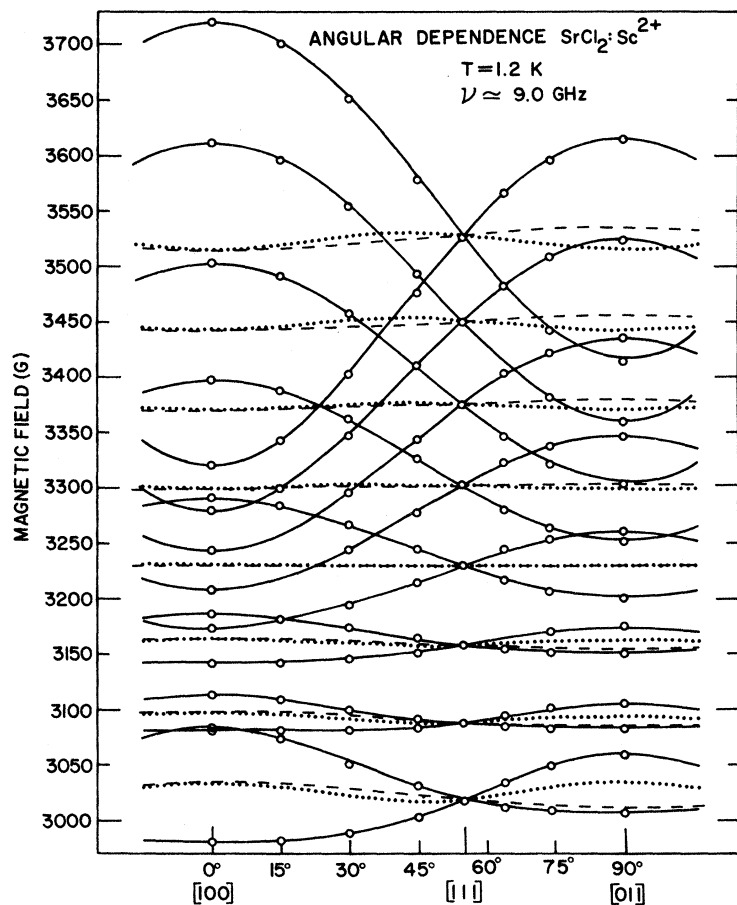


FIG. 7. The angular dependence of the extremes of the EPR spectrum observed for a reduced sample of $\text{SrCl}_2:\text{Sc}^{2+}$. The solid lines were computed using Eq. (3) together with the parameters listed in Table I for Sc^{2+} . The open circles represent the measured extremes. The dashed lines were calculated from Eq. (3) with the $\text{SrCl}_2:\text{Sc}^{2+}$ parameters assuming $\phi=90^\circ$. These dashed lines locate the position of the lines due to averaging by vibronic relaxation for a small relaxation rate. The dotted lines locate the positions of the lines produced by averaging the transitions at the extremes of each envelope. The angular variation of the dashed and dotted lines are a result of the $(qA_2)^2/A_1$ second-order term in Eq. (3).

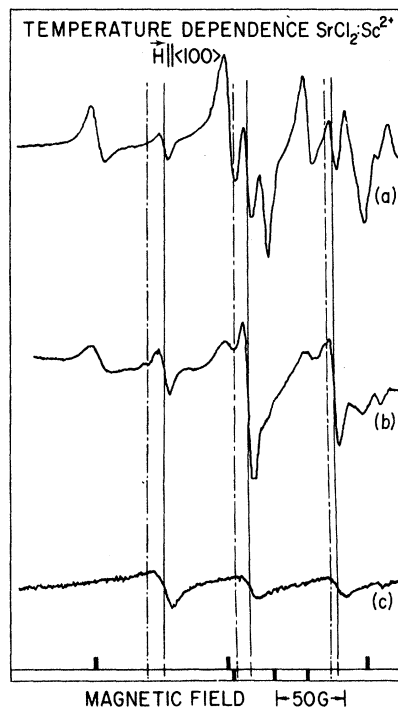


FIG. 8. The temperature dependence of a portion of the EPR spectrum observed for a reduced $\text{SrCl}_2:\text{Sc}^{2+}$ sample. The first derivative of absorption versus magnetic field is shown. The lines produced by rapid vibronic relaxation are identified by solid vertical lines. The broken vertical lines designate the positions of the transitions observed for $\vec{H} \parallel \langle 111 \rangle$. The extremes of each envelope are identified by small vertical bars at the bottom of the figure. The temperature is progressively increasing from (a) to (b) to (c) but values for the temperature were not obtained.

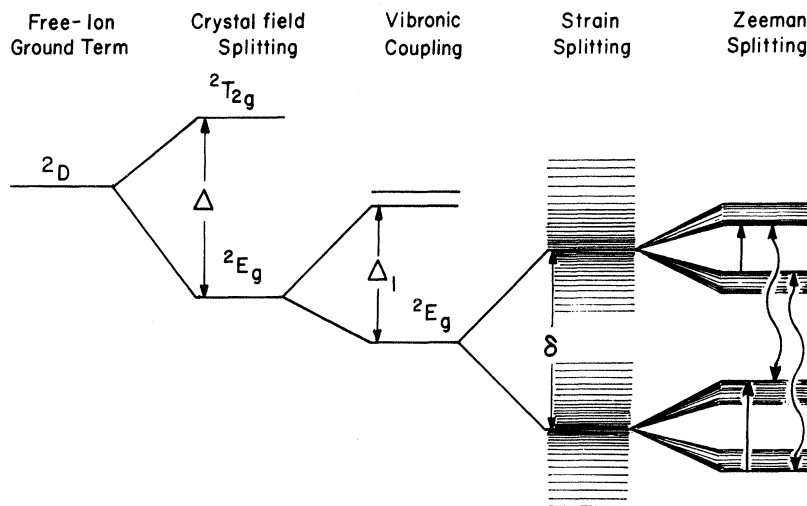


FIG. 9. The schematic energy-level diagram implied by the interpretation of the EPR parameters. The 2D free-ion term is split by the cubic crystal field into 2E_g and ${}^2T_{2g}$ states with the 2E_g lowest. A weak to moderate vibronic interaction results in a series of vibronic states such that the ground vibronic state is also a 2E_g state. The first excited vibronic state is sufficiently far from the ground state to enable one to treat the ground state as an isolated 2E_g state. This state is split by random strains into two Kramer's doublets. The splitting depends on the magnitude of the strain. The Kramer's degeneracy is removed by an applied magnetic field and EPR transitions (represented by straight arrows) are induced by the microwave magnetic field. The wavy arrows represent transitions resulting from vibronic relaxation. They can produce an averaging of a portion of the anisotropic EPR pattern yielding nearly isotropic lines. This type of relaxation should not be confused with spin-lattice relaxation.

should, therefore, be weaker for a $3d$ electron than for a $4d$ or $5d$ electron. In addition, although the ratio $E_{JT}/\hbar\omega$ changes by an order of magnitude, the strain-coupling coefficient qV_s (see Table II) changes only by an approximate factor of 2. Thus, strains on the order of 10^{-4} – 10^{-5} produce splittings of the 2E_g state which are comparable for all three ions. These splittings are sufficiently small that the direct vibronic relaxation rate increases approximately linearly with temperature above 1.3 K. The relaxation rate is proportional to δ^4 , where δ is the strain splitting, and is therefore very sensitive to small variations in δ . In particular, the direct vibronic relaxation rates at $T = 20$ K computed using $\delta = 0.7, 1.3,$ and 1.5 cm^{-1} (see Table II) and the speeds of sound for SrCl_2 ¹¹ imply that the temperature at which the EPR spectrum becomes dominated by the pattern produced by rapid vibronic relaxation differs for the three systems. Since τ^{-1} for $\text{SrCl}_2:\text{Sc}^{2+}$ is at least an order of magnitude less than that for $\text{SrCl}_2:\text{La}^{2+}$, the temperature at which the "averaged" spectrum appears is substantially higher for the Sc-doped crystal. For $\text{SrCl}_2:\text{Y}^{2+}$ the averaging is appreciable at 1.2 K principally because the differences $\nu_+ - \nu_-$ for the averaged transitions are smaller than for Sc^{2+} and La^{2+} .

By dividing the parameters qg_2 , qA_2 , and qQ by

the reduction factor q one obtains the parameters g_2 , A_2 , and Q , which can be combined with g_1 and A_1 in Eqs. (7)–(11) to obtain estimates for the parameters Δ , μ , $\langle r^{-3} \rangle$, κ , and Q_N . These values are listed in Table II. The systematic variations in Δ and $\langle r^{-3} \rangle$ are reasonable. The nuclear magnetic dipole moments and nuclear electric quadrupole moments agree well with the currently accepted values (shown in parentheses in Table II).

The measured EPR parameters for $\text{SrCl}_2:\text{La}^{2+}$, $\text{SrCl}_2:\text{Y}^{2+}$, and $\text{SrCl}_2:\text{Sc}^{2+}$ are all consistent with the following model, which is illustrated in Fig. 9. In an eight-coordinated metal site the 2D free-ion ground term of an ion with one d electron is split by the cubic crystal field into a ground 2E_g state and a ${}^2T_{2g}$ state separated by 10 000 to 20 000 cm^{-1} . The ground vibronic state resulting from a weak to moderate vibronic interaction ($E_{JT}/\hbar\omega \approx 0.1$ to 1.0) is a 2E_g state. The first excited state is on the order of 100 cm^{-1} above the ground state. Owing to large random internal strains (on the order of 10^{-4} – 10^{-5}) the 2E_g state is split into two Kramer's doublets separated in energy by about 1 cm^{-1} . This strain splitting varies from site to site because of the distribution in strain magnitude. The Kramer's degeneracy is removed by the applied magnetic field and the magnitude of the Zeeman splitting depends on the ratio of e_g and e_c strain

components at each site and on the orientation of the applied magnetic field.

The EPR transitions (indicated by solid arrows in Fig. 9) consist of a complex envelope of transitions. The shape of this envelope results from the distribution in e_i/e_0 . Owing to vibronic relaxation (as indicated by wavy arrows in Fig. 9) a portion of the anisotropic spectrum averages to produce a weak nearly isotropic pattern at low temperatures. This pattern increases in intensity with increasing temperature. All features of the EPR spectrum, with the exception of a number of lines observed for $\text{SrCl}_2:\text{Y}^{2+}$ and not associated with Y^{2+} and a single line with $g=2$ observed at high temperatures for Sc^{2+} in SrCl_2 , are consistent with the description given above and are described within experimental error by an effective Hamiltonian for an isolated 2E_g state.

V. SUMMARY

EPR spectra have been observed for $\text{SrCl}_2:\text{Y}^{2+}$ and $\text{SrCl}_2:\text{Sc}^{2+}$ at liquid-helium temperatures. At 1.2 K the spectra were dominated by anisotropic hyperfine patterns whose line shapes and angular dependences were explained using second-order solutions of the effective Hamiltonian for an isolated 2E_g state. Pronounced asymmetries in some of the line shapes observed for $\text{SrCl}_2:\text{Sc}^{2+}$ result from second-order terms previously neglected in the line-shape analysis. The observed variations of

the effective-Hamiltonian parameters are physically reasonable.

Weak nearly isotropic hyperfine lines were observed to coexist with the anisotropic patterns. Variations in the intensities of these weak lines as functions of temperature and magnetic field orientation imply that they result from averaging of a portion of the anisotropic pattern by direct vibronic relaxation. Relaxation rates implied by this interpretation are consistent with those calculated from the strength of the vibronic interaction. This interpretation was further strengthened in the case of $\text{SrCl}_2:\text{Sc}^{2+}$ by the observation of a small predicted anisotropy.

In conclusion, essentially all features of the EPR spectra observed for $\text{SrCl}_2:\text{La}^{2+}$, $\text{SrCl}_2:\text{Y}^{2+}$, and $\text{SrCl}_2:\text{Sc}^{2+}$ are consistent with the model discussed previously and represented schematically in Fig. 9. Observed reductions of certain parameters from the values predicted by crystal-field theory imply the existence of a weak to moderate vibronic interaction, i. e., a dynamic Jahn-Teller effect.

ACKNOWLEDGMENTS

We gratefully acknowledge the valuable technical assistance of E. G. Clardy and the useful comments of B. Dischler on the manuscript. In addition we thank the Office of Naval Research for the contribution of helium used in the initial stages of this work.

*Work supported by the National Science Foundation and the National Aeronautics and Space Administration.

¹Presently at the Institut für Angewandte Festkörperphysik der Fraunhofer Gesellschaft, 78 Freiburg i. Br., West Germany.

²Formerly LTV Research Center.

³H. A. Jahn and E. Teller, Proc. R. Soc. A **161**, 220 (1937).

⁴H. C. Longuet-Higgins, U. Öpik, M. H. L. Pryce, and R. A. Sack, Proc. R. Soc. A **244**, 1 (1958).

⁵F. S. Ham, Phys. Rev. **166**, 307 (1968).

⁶F. S. Ham, in *Electron Paramagnetic Resonance*, edited by S. Geschwind (Plenum, New York, 1972).

⁷M. D. Sturge, in *Solid State Physics*, edited by F. Seitz, D. Turnbull, and H. Ehrenreich (Academic, New York, 1967), Vol.

20.

⁸L. A. Boatner, B. Dischler, J. R. Herrington, and T. L. Estle, Bull. Am. Phys. Soc. **14**, 355 (1969).

⁹J. R. Herrington, B. Dischler, T. L. Estle, and L. A. Boatner, Phys. Rev. Lett. **24**, 984 (1970).

¹⁰J. R. Herrington, T. L. Estle, and L. A. Boatner, Phys. Rev. B **3**, 2933 (1971).

¹¹J. R. Herrington, T. L. Estle, and L. A. Boatner, Bull. Am. Phys. Soc. **16**, 387 (1971); Phys. Rev. B **5**, 2500 (1972).

¹²T. L. Estle, J. R. Herrington, and L. A. Boatner, Bull. Am. Phys. Soc. **16**, 386 (1971).

¹³H. V. Lauer, Jr., K. A. Solberg, D. H. Kuhner, and W. E. Bron, Phys. Lett. A **35**, 279 (1971).